Materials & Design 259 (2025) 114857

Contents lists available at ScienceDirect

Materials & Design

journal homepage: www.elsevier.com/locate/matdes

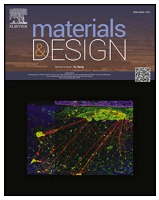

Effect of cold sintering temperatures on the microstructure and mechanical properties of $BaZr_{0.7}Ce_{0.2}Y_{0.1}O_{3-\delta}$ proton conductors

Syed Ali Afzal [a,b,*], Moritz Kindelmann [a], Jürgen Peter Gross [c], Jürgen Malzbender [c], Ruth Schwaiger [c], Olivier Guillon [a,d], Martin Bram [a,e]

[a] Forschungszentrum Jülich GmbH, Institute of Energy Materials and Devices, Materials Synthesis and Processing (IMD-2), Jülich 52425, Germany
[b] Dawood University of Engineering and Technology, Metallurgy and Materials Engineering Department, Karachi 74800, Pakistan
[c] Forschungszentrum Jülich GmbH, Institute of Energy Materials and Devices, Structure and Function of Materials (IMD-1), Jülich 52425, Germany
[d] Jülich Aachen Research Alliance, JARA-Energy, Jülich 52425, Germany
[e] Institut für Werkstoffe, Ruhr-Universität Bochum, Bochum 44801, Germany

ARTICLE INFO

Keywords:
Cold sintering
Proton-conducting ceramics
Mechanical properties
Barium Zirconate cerate
Fracture toughness
Micro-pillar testing

ABSTRACT

Conventional sintering of barium zirconate cerates for proton-conducting ceramic membranes requires high temperatures (1500–1600 °C) and long dwell times (>24 h), leading to Ba evaporation that negatively impacts conductivity. This study adapted the cold sintering process (CSP) to consolidate $BaZr_{0.7}Ce_{0.2}Y_{0.1}O_{3-\delta}$ (BZCY721) ceramics at 150–350 °C, followed by post-thermal treatment at 1300 °C. The cold sintered specimens were characterized for mechanical properties and compared to a specimen sintered conventionally at 1600 °C. The cold sintered materials exhibited a Zr-rich BZY phase ($BaZr_{0.9}Y_{0.1}O_{2.68}$) with smaller grain and pore sizes. The highest density and elastic modulus were found in the specimen cold sintered at 150 °C. Additionally, the hardness of the cold sintered samples was higher than that of the conventional reference due to finer grain size and reduced porosity. Fracture toughness measurements by the Vickers indentation test indicated a value of 1.26 $MPa{\cdot}m^{0.5}$ for cold sintered specimens, compared to 0.93 $MPa{\cdot}m^{0.5}$ for the conventionally sintered specimen. The specimen cold sintered at 150 °C yielded the highest fracture toughness value of 1.48 $MPa{\cdot}m^{0.5}$ by micro-pillar splitting test, along with the total conductivity of 1.48×10^{-4} S/cm at 400 °C, which is comparable to the conventionally processed reference.

1. Introduction

Proton-conducting ceramic materials have been effectively utilized to develop proton-conducting cells (PCC), including fuel and electrolysers as well as membrane reactors [1–4]. Nowadays, solid solutions of barium zirconates ($BaZrO_3$) and barium cerates ($BaCeO_3$) doped with yttrium (Y^{3+}) are broadly studied as potential proton conductors [5,6] due to their high conductivity and improved chemical resistance under H_2O and CO_2 atmospheres [7–9]. However, a major problem with respect to the sintering of BZCY ceramics is the necessary high sintering temperature (1500−1600 °C) coupled with long sintering times (up to 24 h) to fully densify the material. The primary issue induced by high sintering temperatures is the evaporation of Ba^{2+}, leading to the formation of Y and Ce-based impurity phase, which is directly related to a decrease in proton conductivity [9–11]. Various researchers investigated the addition of different sintering aids to BZCY to lower the sintering temperature, particularly NiO [12–15]. However, despite a slight reduction in the sintering temperature (between 100 and 150 °C), the NiO addition was responsible for a decrease in the overall conductivity of the material [16], and the overall sintering temperature is still quite high for consolidation, which also leads to energy losses [17,18].

With the goal of an energy-efficient process for the consolidation of ceramic materials, Randall *et al.* in 2016 [19] developed an ultra-low energy process called the cold sintering process (CSP). The main densification mechanism in CSP is “Pressure solution creep” [20], wherein a ceramic powder, combined with a liquid solvent, undergoes uniaxial pressing under pressures of several hundred MPa while being heated to temperatures not surpassing 350 °C [21,22]. In the context of the cold sintering of BZCY ceramics utilizing water as a liquid sintering aid, Fig. 1 illustrates various stages, highlighting the mechanisms

* Corresponding author at: Forschungszentrum Jülich GmbH, Institute of Energy Materials and Devices, Materials Synthesis and Processing (IMD-2), Jülich 52425, Germany.
E-mail address: s.a.afzal@fz-juelich.de (S.A. Afzal).

https://doi.org/10.1016/j.matdes.2025.114857
Received 14 April 2025; Received in revised form 22 September 2025; Accepted 27 September 2025
Available online 29 September 2025

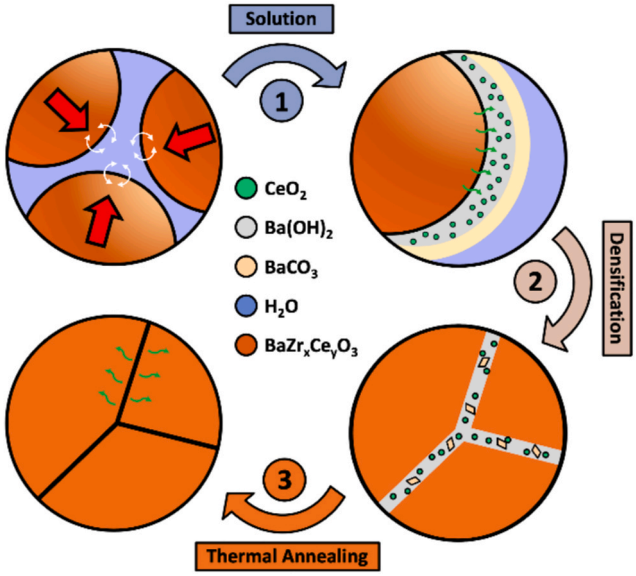

Fig. 1. Schematic diagram of the densification mechanism during cold sintering of BZCY ceramics in the presence of water as liquid sintering aid: Stage 1 shows solution and reprecipitation of chemical species, Stage 2 represents pressure-aided densification, and Stage 3 demonstrates the regaining of the BZCY phase during thermal annealing at elevated temperature. The figure is a reprint from Kindelmann et al. [23].

through which densification occurs during both cold sintering and subsequent thermal treatment.

In Stage 1, referred to as "Solution" in Fig. 1, Ce-based chemical species dissociate by reacting with water under the influence of external pressure, forming $Ba(OH)_2$, $BaCO_3$, and CeO_2 as presented in Eqs. (1) and (2). The impurity compounds remain in the microstructure after water evaporation when cold sintering temperature surpasses the boiling point of water.

$$BaCeO_3 + H_2O \rightarrow Ba(OH)_2 + CeO_2 \quad (1)$$

$$Ba(OH)_2 + CO_2 \rightarrow BaCO_3 + H_2O \quad (2)$$

In the Stage 2 (densification), densification occurs due to applied pressure involving a mechanism that is defined by a stress exponent [24]. The low shear strength found in the precipitates facilitates grain movement in the presence of a high external uniaxial force. Then, the thermal annealing stage, Stage 3, eliminates the impurity phases by promoting diffusion of Y and Ce into the perovskite crystal structure at higher temperatures.

Thabet *et al.* [25] carried out for the first-time cold sintering of Ce-rich $BaCe_{0.8}Zr_{0.1}Y_{0.1}O_{3-\delta}$ proton conducting ceramics, where 83 % relative density was achieved at 180 °C after cold sintering. Further post-annealing treatment at 1200 °C enhanced the density to 93 % with the total conductivity of 4×10^{-2} S/cm at 700 °C [26]. Nonetheless, it is important to mention that the goal of the present study is to carry out the cold sintering of Zr-rich $BaZr_{0.7}Ce_{0.2}Y_{0.1}O_{3-\delta}$ ceramics, which own a better-balanced property profile. The potential to cold sinter $BaZr_{0.7}Ce_{0.2}Y_{0.1}O_{3-\delta}$ with 0.5 wt% of NiO has already been proven by Kindelmann *et al.* [23,27], where the starting powders composed of Ce-rich and Zr-rich BZCY phases showed higher densification during cold sintering as compared to single-phase starting powders. However, post-thermal treatment was found to be prerequisite to regain the BZCY phase and to achieve the aspired functionality as proton-conducting membrane material [27]. In addition, improved proton conductivity and a high relative density of 96 % were achieved when BZCY721 with 0.5 wt% NiO was synthesized by cold sintering at 350 °C, followed by thermal treatment at 1300 °C, when compared with a material sintered conventionally at 1600 °C. The distinctive microstructure achieved by cold sintering at 350 °C and PTT at 1300 °C resulted in the reduction of Ni-based impurity phases at the grain boundaries, thus reducing the core-charge and enhancing electrochemical properties. Hence, due to the optimal combination of density and conductivity, the PTT temperature of 1300 °C was adapted for this study. Nevertheless, microcracking and residual porosity in the microstructure of specimens made from two-phased starting powders remained challenging [23,27]. Stimulated by the superior densification that could be achieved when using two-phased starting powders, it was decided in the current study to observe the effect of lower cold sintering temperatures on the microstructure and mechanical properties.

The mechanical properties of proton-conducting hydrogen separation membranes are of prime importance to ensure reliability and lifespan in the entire temperature range from room to elevated temperatures (300–600 °C). Fractures in the ceramic membrane may result in cell failure because of gas leakage, and the presence of cracks and pores adversely impacts proton conduction by interrupting conductivity paths. To the best of our knowledge, there are no studies on the mechanical properties of BZCY ceramics using cold-sintering as an additional processing step to keep the temperature of the final thermal treatment low. A first indicator of the potential of cold sintering for achieving good mechanical properties at least on the microscale delivers the study of Nur *et al.* [28], where the mechanical performance of ZnO cold sintered at 250 °C was better than the conventionally sintered specimen used as reference. Additionally, 97 % dense ZnO was cold sintered at 120 °C by Lowum *et al.* [29] with a characteristic strength of 64.4 MPa and a Weibull modulus of 8.2 MPa. A recent study on cold sintered ZnO revealed a high density of 98 % and a high biaxial characteristic strength of 88 MPa [30]. Besides, researchers are also working to upscale the cold sintering process. Bang *et al.* [31] demonstrated that the size scale-up can be accomplished on the cold sintered ZnO (from 13 mm diameter to 50 mm diameter) while attaining a density of above 96 %.

The aforementioned results conveyed that enhanced mechanical properties can be achieved when materials are fabricated via cold sintering process (CSP). Therefore, in this study, CSP was adopted to synthesize the ceramic membranes followed by post-thermal treatment (PTT) to regain the main phase to a large extent and to further densify the material. In addition to the microstructure, phase composition, and conductivity analysis, elastic modulus and hardness were derived from micro-indentation tests, thus aiding an assessment of the mechanical integrity of the membrane material. Additionally, the fracture toughness was determined using Vickers indentation and micro-pillar splitting. To demonstrate the advantage of cold sintering as an additional processing step, all of the results were compared with a similar specimen that was conventionally sintered at 1600 °C.

2. Experimental

In this study, a starting powder of chemical composition $BaZr_{0.7}Ce_{0.2}Y_{0.1}O_{3-\delta}$ (BZCY721) was used. In the as-received state, the powder was already calcined at 1100 °C with a 0.5 wt% NiO addition. The specifics of the powder preparation can be found elsewhere [32]. To ensure the two-phase composition of the starting powders composed of Ce-rich and Zr-rich BZCY phases, the powder was again calcined for 5 h at 1300 °C. After calcination, ball milling was carried out in ethanol for 30 mins at the speed of 400 min^{-1}. A planetary ball milling (Retsch PM-400, Germany), Zirconia jars, and Zirconia balls of diameter 3 mm were used for this step. Then the drying was performed at 80 °C for 24 h in air. Afterward, the powder was sieved through a mesh with size of 100 μm.

The cold sintering was carried out under vacuum in a FAST/SPS machine (FAST = field assisted sintering technology, SPS = spark plasma sintering) from FCT Systeme HP-D5, Germany. The tools and die were produced from Mo-based alloy (Trade name TZM, Plansee SE, Austria). For each sample, 2 g powder was weighed and pressed

manually by hand inside the die of 13 mm diameter. Then 5 wt% deionized water was added drop by drop from the top to the hand-compacted green body via a micropipette (Eppendorf, Germany) with no sign of excess water leakage from the die. Then the mixture was pressed inside the die for 60 s using a force of 6 kN. Regarding the temperature for the cold sintering, either 150 °C, 250 °C or 350 °C, respectively, were applied. The pressure was 400 MPa, the heating rate was 20 K/min, and a dwell time of 5 min was maintained during the cold sintering. The post-thermal treatment (PTT) was conducted after cold sintering at 1300 °C for 10 h in air, with a heating and cooling rate of 5 K/min, respectively. To distinguish the materials based on their processing parameters, the nomenclatures established to denote each specimen are presented in Table 1. Additionally, a specimen conventionally sintered at 1600 °C for 5 h in air with a heating and cooling rate of 5 K/min is denoted by Conv_1600. The as-received powder calcined at 1100 °C was used as starting material. Then, 50 MPa pressure was applied to form the green body, and the green body was placed inside a sacrificial powder bed composed of the same powder for the sintering process.

The crystal structure and phase composition of the specimens were determined based on diffraction patterns recorded using an X-ray diffractometer by Brucker D4 Endeavour, USA (Cu-Kα radiation α. The patterns were recorded at room temperature in a 2θ range of 10° to 80° with a step size of 0.02° and a time per step of 0.5 s. The Rietveld analysis of the XRD patterns was carried out using the software TOPAS (Bruker AXS). Further materials' characterization necessitates polished cross-sections. Therefore, the specimens were embedded in epoxy resin, then grinded and polished by SAPHIR 550 (ATM Qness GmbH, Germany). The embedded cross-sections were grinded using 240–2500 grit size SiC paper. The subsequent, polishing was performed with a diamond paste of 6, 3 and 1 μm grain size. The final polishing was done by the SiO_2 particles of 0.5 μm grain size.

Further microstructural analyses were performed based on SEM micrographs of the polished specimens' cross-sections, which were sputtered with Pt. The SEM micrographs were recorded using the GeminiSEM 450 instrument (Zeiss, Germany) using an acceleration Voltage of 8 kV. The elemental composition was determined by EDS (Oxford instruments UK, detector: ULTIM MAX 170). The EDS elemental mapping was carried out using a Merlin SEM instrument (Carl Zeiss Microscopy GmbH, Oberkochen, Germany) using an accelerating voltage of 15 kV. The average porosity was calculated based on image analysis of at least 5 SEM micrographs per specimen using the software ImageJ [33]. The density of specimens was estimated by Archimedes method using deionized water.

For the determination of indentation elastic modulus (E_{IT}) and indentation hardness (H_{IT}), the microhardness testing equipment, FISCHERSCOPE® HC 100 (Helmut Fischer GmbH, Germany) was used. The indentation testing at a load of 1 N was performed by indenting the surface of the polished specimens with a Vickers tip at a loading/unloading rate of 0.05 N/s. For each specimen, a minimum of 10 indents were imprinted across the cross-sections. The E_{IT} was determined based on the standard DIN EN ISO 14577 [34].

The fracture toughness of the specimens was determined using the Vickers indentation method (VIF) as well as the micro-pillar splitting method. For the Vickers indentation method (VIF), denoted by K_{IC_VIF}, the imprints made for the E_{IT} and H_{IT} determination at 1 N load were used [35]. Laser confocal microscope (Model: VK-9700, KEYENCE Germany GmbH) images of the imprints were first made for this purpose. Based on these images the half-diagonal length 'a' and crack length 'l' (measured from the tip of the indent to the crack tip) were quantified. The relationship between l and a for all the indents was found to be $0.25 \leq l/a \leq 2.5$, which confirmed the crack profiles as Palmqvist cracks [35,36]. Therefore, Eq. (3) established by Niihara for Palmqvist cracks [35] was used to compute the K_{IC_VIF}. The equation is given by,

$$K_{IC\_VIF} = 0.035\left(\frac{l}{a}\right)^{-0.5}\left(\frac{H_{IT}}{E_{IT}\,\phi}\right)^{-0.4}\left(\frac{Ha^{0.5}}{\phi}\right) \tag{3}$$

where ϕ is the constraint factor taking the value of 3. For the calculation of fracture toughness from this model, E_{IT} and H_{IT} values obtained for a load of 1 N were used.

For the micro-pillar splitting method represented by K_{IC_MP}, micro-pillars were milled using a Helios 5 DualBeam – FIB-SEM (Thermo Fisher Scientific, Netherlands). The focused ion beam (FIB) milling was performed with a Xe-ion beam at an acceleration voltage of 30 kV. For each specimen, at least 4 micropillars with a diameter and height of 4.2 μm were milled. Micro-pillar splitting was performed using a FT-NMT04 in situ SEM nanoindentation instrument (FemtoTools AG, Schweiz) placed at a tilt angle of 12° in an Apreo 2C SEM instrument (Thermo Fisher Scientific, Netherlands). The SEM imaging was used to align the Berkovich tip to ensure correct positioning of the indentation in the center of the pillar surface. For the SEM imaging an acceleration voltage of 10 kV was chosen. The nanoindentation was performed displacement controlled to a maximum indentation depth of 0.6 μm with a load application time of 2 s.

From the recorded load–displacement data, the critical fracture load 'F' can be determined by a 'pop-in' event. The 'pop-in' events were characterized by a sharp decrease in the load in the representative load–displacement curves because of the crack formation. The K_{IC_MP} can then be calculated using Eq. (4),

$$K_{IC\_MP} = \gamma \cdot \frac{F}{D^{1.5}} \tag{4}$$

where γ is a pre-factor which can be estimated based on the ratio of the materials' elastic modulus and hardness. D is the diameter of the micro-pillar i.e. 4.2 μm. To estimate the γ for each micro-pillar, the elastic modulus and hardness at low loads was determined by continuous stiffness measurements using a Berkovich tip (Nano Indenter G200X, KLA Instrument). Per sample at least 15 continuous stiffness measurements were carried out from 1 mN load to a maximum load of 50 mN at a constant displacement rate.

The conductivity of the specimens was evaluated by electrochemical impedance spectroscopy (EIS, Novocontrol Technologies Alpha-A High Performance Frequency Analyzer, Germany). Silver electrodes were painted on polished specimens, dried, and subsequently sintered at 850 °C for 10 min in air. Impedance measurements were carried out within the temperature range of 400–200 °C in wet 2.9 % H_2/Ar ($p(H_2O)$ ≈0.025 bar), and at frequencies ranging from 0.1 Hz to 10 MHz. The impedance data was fitted using a series of equivalent circuits consisting of parallels of a resistance and a constant phase element (R||CPE), being associated to the bulk, grain boundary, and electrode response. The brick layer model was used to calculate the conductivities from optimized fits in RelaxIS 3 (rhd instruments, Germany). The total conductivity was obtained using Eq. (5),

$$\sigma_t = \frac{1}{(R_b + R_{gb})}\frac{l}{A} \tag{5}$$

where σ_t is the total conductivity, R_b the bulk resistance, R_{gb} the grain boundary resistance, l the thickness of the measured pellet, and A the diameter of the pellet.

Table 1
Nomenclature adapted to differentiate materials based on their processing parameters.

Specimen	Cold sintering temperature (°C)	Dwell time during cold sintering (mins)	PTT temperature (°C)	PTT time (h)
PTT_150	150	5	1300	10
PTT_250	250	5	1300	10
PTT_350	350	5	1300	10
Conv_1600	Conventionally sintered at 1600 °C for 5 h			

3. Results and discussion

The XRD diffractograms of the specimens are presented in Fig. 2. The relative amount and lattice parameters of different phases are presented in Table 2. Irrespective of the cold sintering temperature, all specimens contained an additional Zr-rich BZY phase alongside a pure BZCY721 phase after PTT. The space group of all the detected phases was *Pm-3m*. A similar Zr-rich BZY phase was present in the starting powders after calcination at 1300 °C (Supplementary Fig. S1). The Conv_1600 specimen, though, did not show any impurity phase and was comprised of the BZCY721 targeted phase because of the higher sintering temperature of 1600 °C. For cold sintered specimens, the PTT temperature of 1300 °C was not enough to stimulate the amalgamation of Zr-rich BZY phase into a single perovskite crystal lattice, owing to the refractory nature of Zr, demanding a higher temperature for the diffusion of Zr^{4+} ions. Although it has been demonstrated previously that after cold sintering, increasing the PTT temperature to 1500 °C and 1600 °C promoted the incorporation of Zr-rich BZY phase into a single BZCY721 phase, the proton-conductivity of the specimens was inferior as compared to the material thermal treated at 1300 °C [23]. In addition, our results reveal that the lowering of the cold sintering temperature did not eliminate the Zr-rich BZCY secondary phase, and it was inevitable when the starting powder with dual-phase composition and a PTT at only 1300 °C was applied. Furthermore, the highest amount of Zr-rich BZY phase was detected by Rietveld analysis in the PTT_250 specimen, as presented in Table 2. The Zr-rich BZY phase detected in all the cold sintered specimens displayed smaller lattice parameters as compared to the BZCY721 phase.

The SEM micrographs of all the specimens are presented in Fig. 3. The microstructures of the specimens prepared by cold sintering were comprised of two impurity phases other than the Zr-rich BZY secondary phase. In the case of the PTT_150 specimen, the impurity phase marked by red circles in Fig. 3a seemed to be segregated and protruding from the polished surface. However, this impurity phase was more homogeneously dispersed in the PTT_250 and PTT_350 specimens. Additionally, another impurity phase marked by green circles in Fig. 3a was found to be embedded between the grains. A similar impurity phase was also observed in the PTT_250 and PTT_350 specimens when the images were captured at higher magnification, as shown in Supplementary Fig. S2. EDS point analysis was carried out on the locations of the above-mentioned impurity phases in the PTT_150 specimen to identify the chemical elements of the impurities (see Fig. 4a).

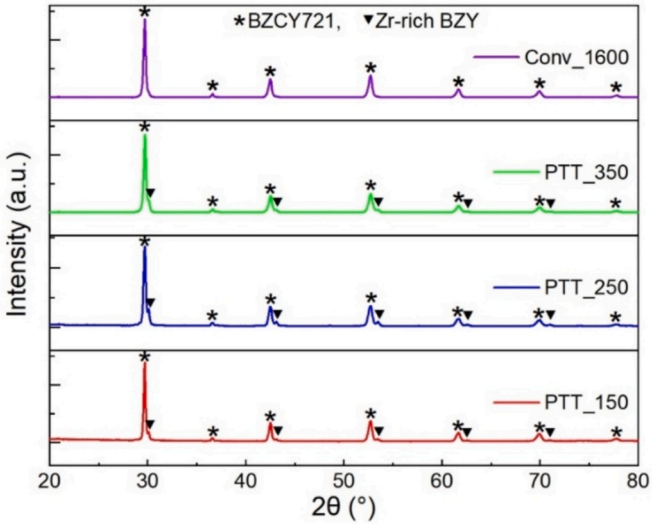

Fig. 2. XRD diffractograms of PTT_150, PTT_250, PTT_350, and Conv_1600 specimens from 20° to 80° range showing the main peaks of the BZCY721 ($BaZr_{0.7}Ce_{0.2}Y_{0.1}O_{3-\delta}$) phase along with Zr-rich BZY ($BaZr_{0.9}Y_{0.1}O_{2.68}$) secondary phase.

Table 2
The relative amount and lattice parameter (a) of the targeted BZCY721 phase and Zr-rich BZY secondary phase.

Specimen	Targeted BZCY721 phase		Zr-rich BZY secondary phase	
	Amount (wt. %)	a (Å)	Amount (wt. %)	a (Å)
PTT_150	94	4.257(3)	6	4.200(9)
PTT_250	87	4.256(3)	13	4.199(6)
PTT_350	96	4.256(2)	4	4.197(6)
Conv_1600	100	4.251(1)	0	–

The EDS spectrum extracted from spot-1 (Fig. 4b) revealed a high intensity of Ni in the region where the impurity phase was segregated. This observation referred to the presence of a Ni-based impurity in the microstructure, which remained undissolved in the perovskite structure after PTT at 1300 °C. Moreover, the EDS spectrum at spot-2, showed a high concentration of Yttrium. Several studies where NiO was used as a sintering aid during the conventional sintering of BZCY ceramics discussed the presence of a secondary BaY_2NiO_5 phase, which aided the densification and enhanced grain growth at lower temperatures [14–16,37,38]. Tong *et al.* illustrated that the BaY_2NiO_5 phase started forming around 900 °C in $BaZr_{0.8}Y_{0.2}O_{3-\delta}$ ceramics with 2 wt% NiO, which then liquified around 1450–1500 °C. In addition, the BaY_2NiO_5 phase started to decompose at temperatures higher than 1200 °C resulting in the formation of NiO and Y_2O_3 as shown in Eq. (6) [37,39]:

$$BaY_2NiO_5 \rightarrow BaO + NiO + Y_2O_3 \quad (6)$$

At the PTT temperature of 1300 °C, the bulk material was unable to completely incorporate the Ni and Y into the BZCY perovskite crystal structure in our specimens, which resulted in the observed NiO and Y_2O_3 impurity phases. On the other hand, no impurity phase was observed in the microstructure of the Conv_1600 specimen in Fig. 3d, which proved that at 1600 °C, Ni and Y completely dissolved in the crystal structure. Nevertheless, the absence of these impurity phases in the XRD data could also be due to the detection limit of the equipment, which was 1–2 %.

The PTT_350 specimen revealed in addition the presence of microcracks (red arrows in Fig. 3c). The presence of cracks during the cold sintering of BZCY ceramics was also reported in the previous studies [25–27,40]. When water is used as a sintering aid for the cold sintering of BZCY, $Ba(OH)_2$ is initially formed due to the reaction of water with $BaCeO_3$, which then further reacts with CO_2 to form $BaCO_3$, as shown previously in Eq. (1) and Eq. (2). Moreover, the $BaCO_3$ can also be formed when $BaCeO_3$ directly reacts with CO_2 as shown in Eq. (7). The origin of CO_2 in our experiments was most likely the graphite sheet that was placed between the powder and the TZM tool during the cold sintering. Alternatively, it might come from the atmosphere.

$$BaCeO_3 + CO_2 \rightarrow BaCO_3 + CeO_2 \quad (7)$$

The presence of $BaCO_3$ as an impurity phase in the as cold sintered BZCY was also discussed previously [23,25–27]. During PTT at higher temperatures, the evaporation of remaining moisture in the as cold sintered state or the mechanical stresses generated by $BaCO_3$ to the surrounding matrix is likely the main cause of crack formation. Furthermore, inhomogeneous densification in the cold sintered specimens was detected where certain zones contained a high number of residual pores, while other zones were almost dense, revealing negligible porosity. This was especially the case in the PTT_150 and PTT_250 specimens as shown in Fig. 3a and b, respectively. Fig. 5 shows EDS elemental mapping carried out to investigate the reasons for the inhomogeneous densification in the cold sintered specimens and apparent a little more uniform pore distribution in the conventionally sintered specimen.

A high concentration of Y was present in the porous areas in cold sintered specimens as shown in Fig. 5a–c. Different researchers also

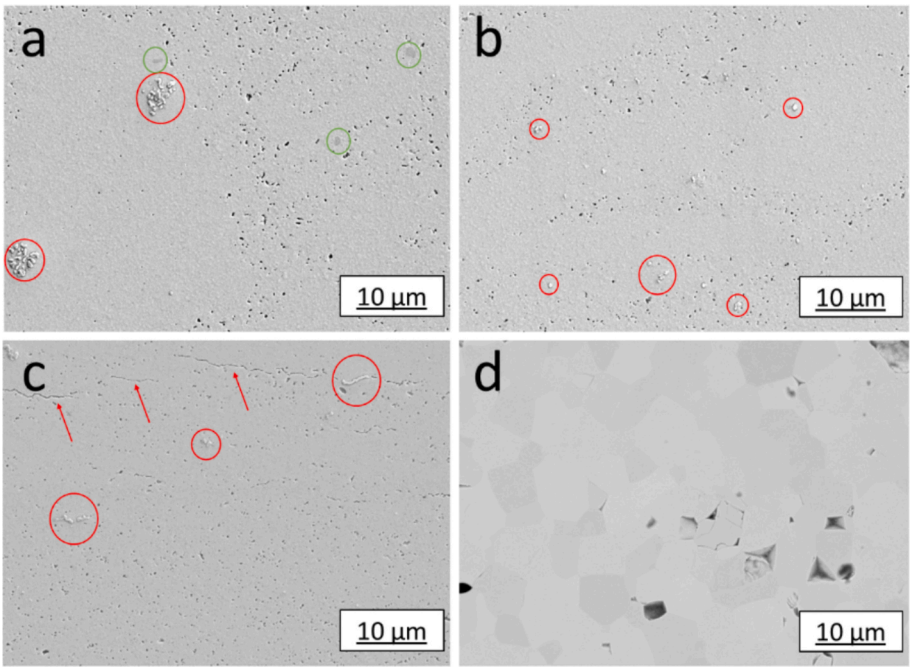

Fig. 3. Secondary electron SEM images of PTT_150 (a), PTT_250 (b), PTT_350 (c), and Conv_1600 (d) specimens. The red circles and green circles mark the NiO and Y_2O_3 impurity phases, respectively. Red arrows highlight micro-cracks in the PTT_350 specimen. (For interpretation of the references to colour in this figure legend, the reader is referred to the web version of this article.)

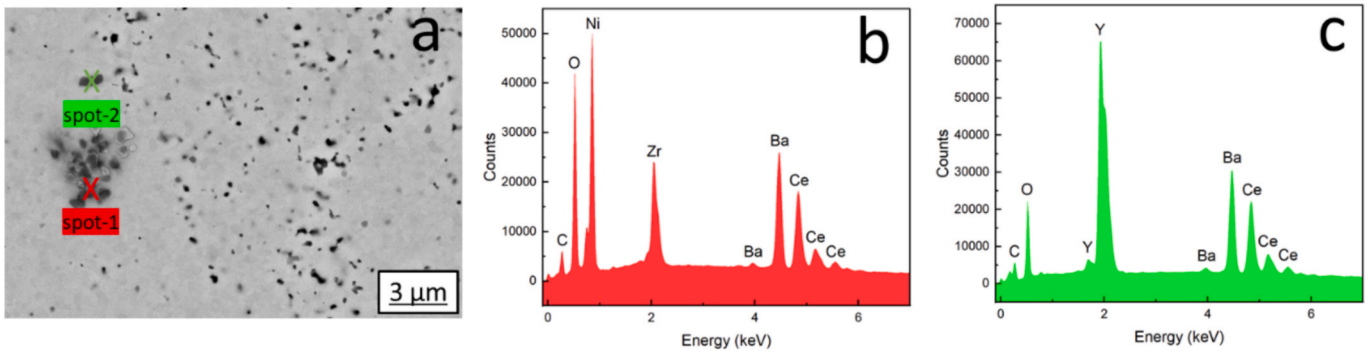

Fig. 4. Point EDS analysis carried out at spot-1 and spot-2 marked by red cross and green cross in the PTT_150 specimen, respectively (a). EDS spectrum extracted from spot-1 (b) showed a Ni-rich phase whereas EDS spectrum at spot-2 (c) showed a high concentration of a Y-rich phase, respectively. (For interpretation of the references to colour in this figure legend, the reader is referred to the web version of this article.)

highlighted the negative effect of Y on the densification of BZCY-based proton conductors. A study on BZY ceramics showed that an increase in the Y content on $BaZr_{1-x}Y_xO_{3-\delta}$ led to a decrease in the density and elastic modulus of the material [41]. Zeng *et al.* [71] also investigated the effect of Y quantity in the conventionally sintered $BaZr_{0.8-x}Ce_{0.2}Y_xO_{3-\delta}$ proton-conducting ceramics and reported a decrease in relative density with the increase in the amount of Y. Moreover, the increase in the Y quantity was found to be correlated with the high number of pores in the microstructures [42]. Essentially, the existence of the secondary Y_2O_3 phase influenced mass transfer during post-treatment (PTT) by locating itself between the grains. Given the relatively low PTT temperature of 1300 °C and the apparent similar grain size of the Y_2O_3 impurity phase when compared with surrounding grains in the cold sintered specimen (Fig. 4a), the driving force for further growth was minimal, mainly due to the reduced surface energy, hindering the pores closure adjacent the Y_2O_3 phase. Furthermore, the inhomogeneous distribution of the Y-based impurity phase was likely the result of the Y gradient in the calcined powder before cold sintering. On the contrary, despite being sintered from the same as-received starting powder, the Conv_1600 specimen did not show clearly pronounced dense and porous regions, and the Y was found to be uniformly distributed in the microstructure as shown in Fig. 5d. The reason for this was most likely the higher sintering temperature which promoted grain growth and allowed Y to become homogeneously distributed throughout the specimen. Therefore, it could be concluded that the non-homogeneous distribution of 10 mol.% Y did not have significant effect on the pore distribution during conventional sintering, but played a major role when the specimens were prepared by cold sintering.

Finally, the grain size of the Conv_1600 specimen was found to be visibly larger than the cold sintered specimens. The apparent pore size of the cold sintered specimens was significantly smaller when compared with the conventionally sintered specimen, which has been reported in literature previously [23,27,28].

The density and porosity values of the specimens are given in Fig. 6. The apparent density of the PTT_150 specimen was found to be the highest, which showed that our optimized cold sintering parameters developed specimens relatively denser than the conventional sintering route. The porosity data in Fig. 6 showed that the apparent porosity in

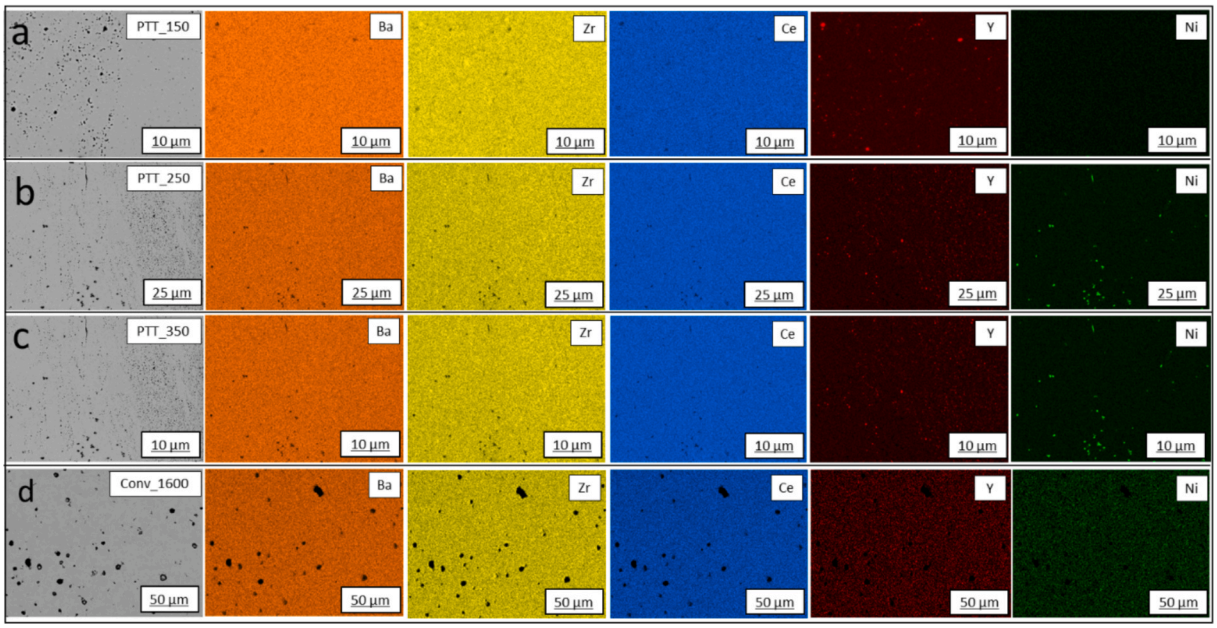

Fig. 5. EDS mapping of cold sintered (a-c) and conventionally sintered (d) specimens. Y segregation was observed in the porous areas in the cold sintered specimens (a-c), while Y was homogeneously distributed in Conv_1600 specimen (d).

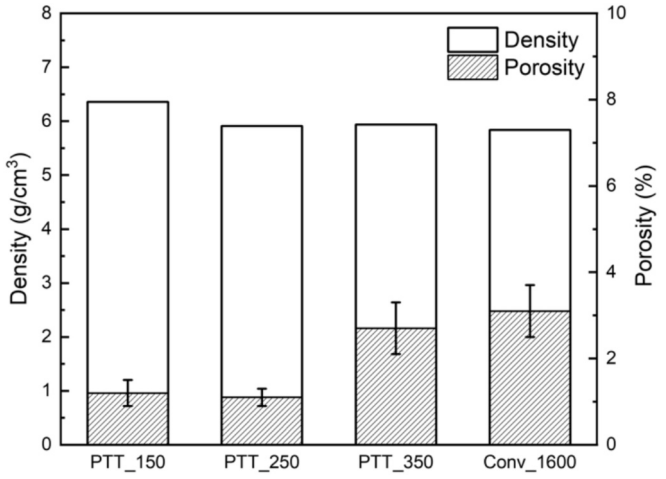

Fig. 6. Archimedes density and porosity in PTT_150, PTT_250, PTT_350, and Conv_1600 specimens. PTT_150 specimen showed the highest apparent density among all the specimens. Despite the lowest apparent porosity, the PTT_250 specimen showed the lowest apparent density among the cold sintered specimens, most likely because of the highest amount of less-dense Zr-rich BZY phase.

the PTT_350 specimen (≈2.7 ± 0.6 %) was higher than the apparent porosity of PTT_150 (≈1.2 ± 0.3 %) and PTT_250 (≈1.1 ± 0.2 %) specimens. However, one contradicting observation was that despite the lowest apparent porosity in the PTT_250 specimen, its apparent density was almost similar to the PTT_350 specimen, which showed more than twice the porosity content as the PTT_250 specimen. In principle, the low porosity should have translated to the high density, which was not the case here. One explanation for the lower apparent density of the PTT_250 specimen despite the low apparent porosity could be the Zr-rich BZY secondary phase. As previous studies on BZCY have shown, an increase of the porosity with a simultaneous reduction of the density can be linked to increasing amounts of Zr [43–46]. The reason behind is that the Zr-rich BZCY compositions require a higher sintering temperature of around 1450 °C compared to what was used in this study [37,47]. The PTT temperature of 1300 °C in the current study might not have been enough to densify the Zr-rich BZY phase. Therefore, it can be concluded that despite the lowest apparent porosity, the highest proportion of less-dense Zr-rich BZY secondary phase contributed to the overall reduction in the apparent density of the PTT_250 specimen.

In addition, the Conv_1600 specimen showed the lowest apparent density and highest amount of apparent porosity among all the specimens. Since the pores are still connected to the grain boundaries (see Fig. 3d), further optimization of sintering parameters might enable to further reduce the residual porosity in this case of conventional sintering.

The elastic modulus (E_{IT}) and hardness (H_{IT}) values of the specimens obtained from indentation tests at 1 N load are presented in Fig. 7. The

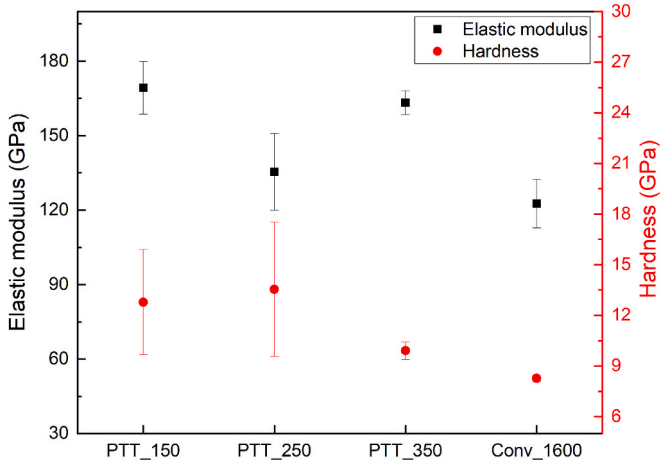

Fig. 7. Elastic modulus (E_{IT}) and hardness (H_{IT}) of specimens after PTT (black squares and red circles respectively) at a load of 1 N. PTT_150 specimen showed the highest elastic modulus due to the highest density. PTT_250 specimen showed the highest hardness because of the lowest porosity, but a lower elastic modulus due to the presence of the highest amount of Zr-rich BZY phase. High scatter in the hardness values in PTT_150 and PTT_250 specimens was the result of the inhomogeneous pore distribution. (For interpretation of the references to colour in this figure legend, the reader is referred to the web version of this article.)

PTT_150 specimen revealed the highest E_{IT} of 169 ± 10 GPa among all the specimens, which can be attributed to the lower porosity of this specimen, which (as previously discussed) is due to a reduction of the cold sintering temperature. The E_{IT} of PTT_250 specimen corresponded to 135 ± 15 GPa, which was found to be lower compared to the E_{IT} of PTT_350 (163 ± 5 GPa) despite exhibiting a lower porosity as shown in Fig. 6. This observation does not correspond well with the established concept that the elastic modulus decreases with increasing porosity [48,49], hence additional influences should be considered. One possible explanation for the low E_{IT} value of the PTT_250 specimen could be the presence of the less dense Zr-rich BZY secondary phase, which has its highest concentration in the PTT_250 specimen. The high concentration of less dense Zr-rich BZY phase was most likely the reason for the overall reduction of the elastic modulus in this specimen. Finally, the E_{IT} of the conventionally-sintered specimen was found to be the lowest due to the lowest apparent density and highest apparent porosity [49–51].

The H_{IT} of the PTT_250 specimen was found to be 13.5 ± 3.9 GPa, which was the highest among all the specimens. Since hardness is also directly linked with the presence of porosity in a material [52], the hardness results validated the porosity figures within a reasonable error of uncertainty. In addition, the lowest hardness among the cold-sintered specimens of 9.9 ± 0.5 GPa has been attributed to PTT_350 specimen, which also showed the highest porosity. A large scatter in the hardness values was observed in the case of PTT_150 and PTT_250 specimens, which might have been related to the inhomogeneous distribution of pores in these specimens. Fig. 8 shows the Vickers imprints that were used to calculate the E_{IT} and H_{IT} values. The diagonal length of the indent (=2·a) in the cold-sintered specimens was between 14–15 μm as shown in Table 3. The location of the indents had an enormous effect on the hardness values because the size by the indent was similar to the size of the dense and porous regions, especially in the PTT_150 and PTT_250 specimens, giving lower values for the porous regions, and higher values for the dense regions. However, the porosity was distributed rather uniformly in the PTT_350 specimen which translated to the lower scattering of the hardness values. For the Conv_1600 specimen, the indents were made specifically in the areas without large pores directly beneath the indenter to minimize the effect of large pores on the experiment, hence the minimum scatter results. In general, the hardness values of the cold-sintered specimens are higher compared to the conventionally-sintered one (Conv_1600), which can be attributed to various factors such as higher porosity, lower density, and larger grain sizes in the case of the conventionally-sintered specimen [49,53,54].

Table 3
Half-diagonal length 'a', radial crack length 'l', l/a ratio, and fracture toughness 'K_{IC_VIF}' calculated from the Vickers indents at 1 N load. 'l' represents the average length.

Specimen	a (μm)	l (μm)	l/a	K_{IC_VIF}
PTT_150	7.2 ± 0.2	13.8 ± 1.4	1.92 ± 0.19	1.26 ± 0.07
PTT_250	7.1 ± 0.2	11.8 ± 0.8	1.67 ± 0.15	1.26 ± 0.08
PTT_350	7.5 ± 0.1	12.8 ± 1.5	1.71 ± 0.22	1.15 ± 0.09
Conv_1600	8.4 ± 0.2	15.8 ± 1.4	1.89 ± 0.17	0.93 ± 0.04

The Vickers indentation-based fracture toughness (K_{IC_VIF}) results of the specimens along with the half-diagonal length 'a', radial crack length 'l', and l/a ratio are presented in Table 3. The PTT_150 and PTT_250 specimens yielded similar K_{IC_VIF} of 1.26 MPa·m$^{0.5}$, which can mainly be attributed to the low porosity and fine grain size of the materials [55,56]. The K_{IC_VIF} of the PTT_350 specimen (1.15 MPa·m$^{0.5}$) was slightly lower than the PTT_150 and PTT_250 specimens, probably because of the pre-existing micro-cracks (red arrows in Fig. 8c) as well as the higher porosity. The K_{IC_VIF} of the Conv_1600 specimen was found to be the lowest compared to the cold sintered specimens, which showed that the materials prepared by the combination of cold sintering and PTT had superior mesoscale fracture toughness compared to the conventionally sintered material, which is a promising result. The low K_{IC_VIF} of the Conv_1600 specimen was primarily due to the higher porosity and the larger grain size of the material. As highlighted by the red dashed circle in Fig. 8d, the large pore facilitated the crack growth by providing a low-energy growth path in Conv_1600 specimen. Nevertheless, the calculation of fracture toughness from the Vickers indentation test is

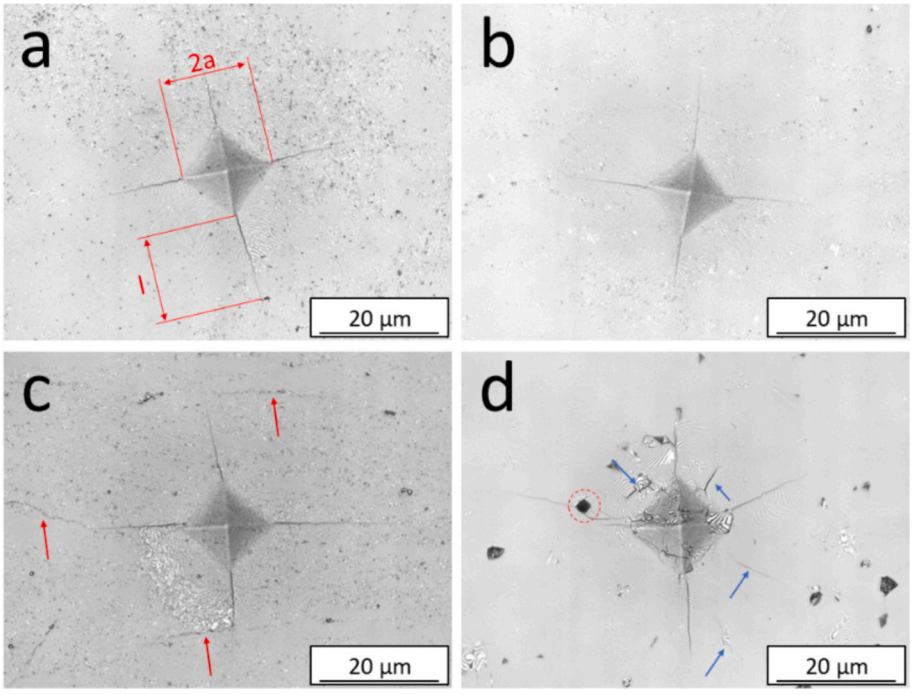

Fig. 8. Micrographs of the Vickers imprints after applying a load of 1 N on PTT_150 (a), PTT_250 (b), PTT_350 (c), and Conv_1600 (d) specimens, all images obtained by Laser scanning microscope. Red arrows point towards the pre-existing micro-cracks in (c). Blue arrows indicate the secondary cracks around the indent in (d). The red dashed circle in (d) represents crack growth along the pore due to the low-energy path. (For interpretation of the references to colour in this figure legend, the reader is referred to the web version of this article.)

highly dependent on the accuracy of measuring the half-diagonal length of the indents and the crack lengths, thus human error also has an influence on the final calculated values [57]. Moreover, the choice of the equation in accordance with the crack profile used for the calculation of the K_{IC_VIF} also impacts the outcome [58]. Therefore, although being widely used, K_{IC_VIF} must be considered mainly to serve as a comparison among the specimens, revealing tendencies, not merely as the exact figures. Thus, in addition, micro-pillar splitting tests were carried out on all specimens to determine the fracture toughness without the need to manually measure the crack lengths generated after the indentation on the specimen's surface [59]. The main advantage of this technique over VIF is the elimination of post-test image analysis to assess the indent features. Furthermore, the residual stresses are also released and do not affect the test results when the ratio of height to diameter of the pillars is greater than 1.0 [60].

Fig. 9 presents the examples of micro-pillars after splitting and the representative load–displacement curves of 4 pillars for all specimens. The micro-pillars were milled specifically in the apparent dense areas in the specimens to minimize the direct influence of porosity on the pillar fracture. However, the homogeneously distributed small-sized pores in the PTT_350 specimen constrained the formation of micro-pillar completely devoid of pores, so the pillars milled in the PTT_350 specimen also contained small-sized pores as highlighted by orange circles in Fig. 9f.

The critical fracture load '*F*' was identified from a 'pop-in' event in the representative load–displacement curves highlighted by red arrows in Fig. 9a. A summary of the *F* for each pillar and the calculated fracture toughness 'K_{IC_MP}' values are summarized in Table 4.

As shown in Table 4, the highest K_{IC_MP} value of 1.48 ± 0.10 MPa·m$^{0.5}$ was observed for the PTT_150 specimen. Moreover, the K_{IC_MP} value for the PTT_250 specimen was 1.38 ± 0.14 MPa·m$^{0.5}$, although slightly less than the PTT_150 specimen, the results were similar and agree within the limit of experimental uncertainty. However, the K_{IC_MP} of the PTT_350 specimen was 1.31 ± 0.08 MPa·m$^{0.5}$, which was the lowest among the cold sintered specimens, corroborating the findings previously discussed for VIF. The Conv_1600 specimen yielded K_{IC_MP} of 1.40 ± 0.04 MPa·m$^{0.5}$, which was equivalent to the K_{IC_MP} values of specimens prepared by cold sintering resulted in contradicting the results of the VIF tests. The reason for the K_{IC_MP} value for the Conv_1600 specimen being similar to the cold sintered specimens, was the absence of pores within the micro-pillars. Another important observation was the higher fracture toughness values for all the specimens in the case of the micro-pillar splitting test when compared with the VIF, as shown in Fig. 10.

Table 4
Details of the critical fracture load '*F*' at which pillars fractured for each specimen along with fracture toughness of the individual pillar 'K_{IC_MP}', and the average K_{IC_MP} of each specimen.

Specimen	Pillar No.	*F* (mN)	K_{IC_MP} (MPa·m$^{0.5}$)	Average K_{IC_MP} (MPa·m$^{0.5}$)
PTT_150	1	14.08	1.34	1.48 ± 0.10
	2	15.12	1.44	
	3	16.20	1.54	
	4	16.90	1.61	
PTT_250	1	13.89	1.26	1.38 ± 0.14
	2	14.04	1.27	
	3	17.70	1.62	
	4	14.37	1.36	
PTT_350	1	13.47	1.25	1.31 ± 0.08
	2	13.79	1.28	
	3	13.39	1.25	
	4	15.42	1.44	
Conv_1600	1	14.61	1.46	1.40 ± 0.04
	2	13.42	1.34	
	3	11.93	1.41	
	4	13.75	1.38	

This observation was previously discussed by Zhou *et al.* [61], where the microscale fracture toughness measured by the micro-pillar splitting test was found to be higher than the mesoscale fracture toughness, which was measured by VIF for $BaCe_{0.65}Zr_{0.2}Y_{0.15}O_{3-\delta}$ sintered conventionally at 1500 °C. This improvement in the fracture toughness was a result of concentrated load application which was restricted to a well-defined surface area as well as the absence of porosity in the tested region, which also explains the increase in K_{IC_MP} values in our study. Additionally, results of the low load indentation (at 10 mN load provided in Supplementary Fig. S4) indicated that the E_{IT} and H_{IT} values of different specimens agree within the limits of experimental uncertainty,

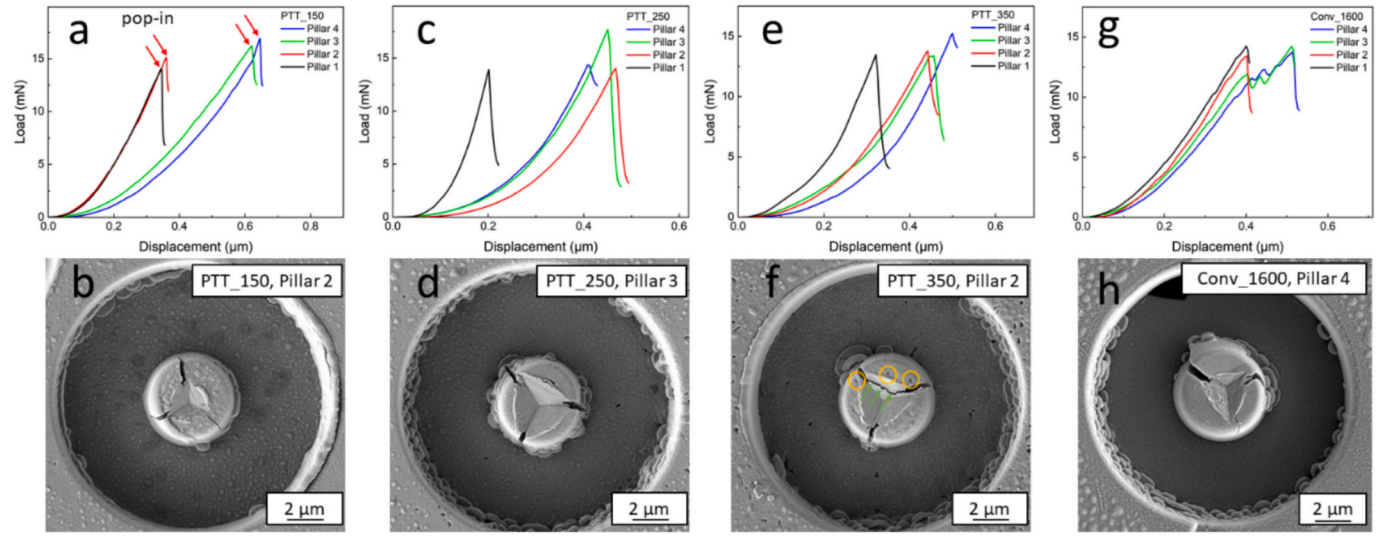

Fig. 9. Representative load–displacement curves along with SEM images of a micro-pillar after the indentation for PTT_150 (a, b), PTT_250 (c, d), PTT_350 (e, f), and Conv_1600 (g, h) specimens, respectively. The critical fracture load '*F*' was determined by the pop-in event pointed out by red arrows in (a). Small-sized pores and a crack inside the indent were highlighted by orange circles and green arrows respectively inside pillar 2 in the PTT_350 specimen (f). The images of the remaining 3 micro-pillars after splitting for all specimens are given in the supplementary Fig. S3. (For interpretation of the references to colour in this figure legend, the reader is referred to the web version of this article.)

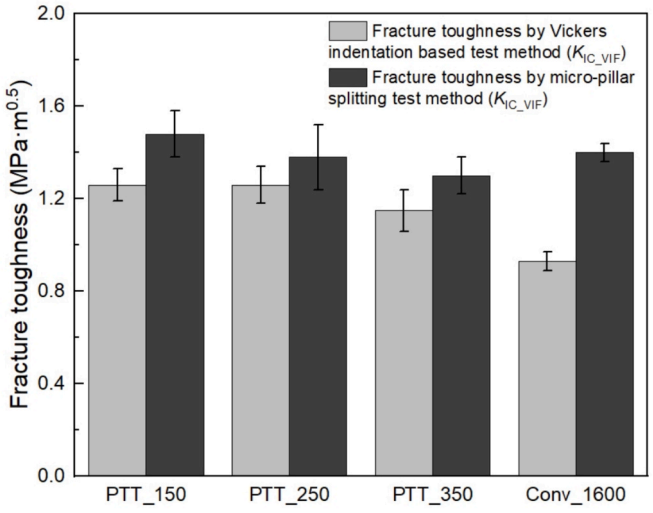

Fig. 10. A comparison of fracture toughness values as estimated by Vickers indentation-based fracture toughness method 'K_{IC_VIF}' and micro-pillar splitting test method 'K_{IC_MP}'.

being $E_{IT} \approx 194$ GPa and $H_{IT} \approx 12.9$ GPa thus indicating, in agreement with the results of the micro-pillar tests that the basic materials' mechanical properties are independent of the processing and results obtained at higher loads and the apparent differences are mainly associated with the effect of undulations, i.e. pores and/or micro-cracks.

Finally, the total conductivity (σ_t) of all specimens is illustrated in Fig. 11. The results indicated that among the cold sintered specimens, reducing the cold sintering temperature significantly enhanced conductivity, with the PTT_150 specimen achieving the highest conductivity of 1.48×10^{-4} S/cm at 400 °C. This increase in conductivity can be directly attributed to improvements in density, a reduction in porosity, and the elimination of cracks, all of which can obstruct proton conduction pathways. However, the total conductivity of the Conv_1600 specimen was greater than that of the cold sintered specimens across the entire testing temperature range. The relatively low conductivity of the cold sintered specimens is linked to the Zr-rich BZY phase and impurity

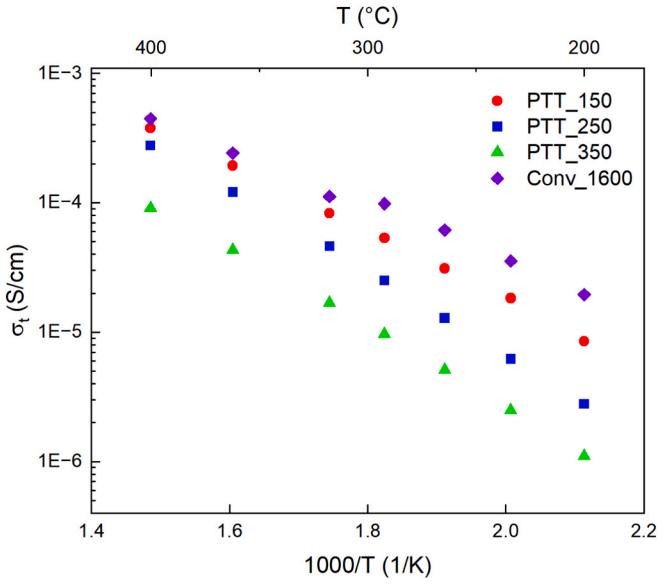

Fig. 11. Total conductivity (σ_t) of specimens measured via impedance spectroscopy in wet 2.9%H_2/Ar. The conductivity values for the PTT_350 and Conv_1600 specimens are reprinted from the works of Kindelmann et al. [23,62].

compounds of Ni and Y. The decrease in oxygen vacancies, resulting from the removal of Y from the BZCY lattice, could have been a primary factor contributing to the lower conductivity of the cold sintered specimens. Nonetheless, the conductivity of the PTT_150 specimen at the working temperature of membranes was on par with the conventionally sintered specimen (4.46×10^{-4} S/cm at 400 °C), while also demonstrating superior overall mechanical performance.

4. Conclusion

In our current study, the $BaZr_{0.7}Ce_{0.2}Y_{0.1}O_{3-\delta}$ (BZCY721) proton-conducting ceramic membranes with 0.5 wt% NiO were prepared by cold sintering and subsequent post-thermal treatment (PTT). As reference, another specimen was sintered conventionally at 1600 °C to benchmark the properties, especially the mechanical performance, with the cold sintered specimens. The XRD results showed that the cold sintered specimens possessed an additional Zr-rich BZY phase ($BaZr_{0.9}Y_{0.1}O_{2.68}$) with smaller lattice parameters than the targeted BZCY721 phase. SEM and EDS analysis showed the presence of NiO and Y_2O_3 impurity phases in the cold sintered specimen along with the smaller grain and pore size. Moreover, the highest density of 6.38 g/cm^3 was observed for the specimen cold sintered at 150 °C. On the other hand, the conventionally sintered specimen revealed the lowest density of 5.84 g/cm^3. A non-uniform densification was observed in specimens cold sintered at 150 °C and 250 °C due to Y_2O_3 segregation. The elastic modulus and hardness of cold sintered specimens were also higher than the specimen sintered conventionally with highest elastic modulus of 169 ± 10 GPa and highest hardness of 13.5 ± 3.9 GPa when cold sintering was carried out at 150°C and 250 °C respectively. The reduction in the elastic modulus and hardness in the conventionally sintered specimen was a result of larger grain size and higher porosity. The specimens cold sintered at 150°C and 250°C also displayed high fracture toughness value of 1.26 MPa·m$^{0.5}$ as derived by Vickers indentation-based method as compared to the value of 0.93 ± 0.04 MPa·m$^{0.5}$ obtained for the specimen sintered conventionally. The highest fracture toughness of 1.48 ± 0.10 MPa·m$^{0.5}$ as obtained from micro-pillar splitting testing was observed for the specimen cold sintered at 150°C. The fracture toughness from micro-pillar splitting test of the conventionally sintered specimen (1.40 ± 0.04 MPa·m$^{0.5}$) was also found to be similar to the cold sintered specimens. However, specimen cold sintered at 350°C showed the lowest fracture toughness of 1.31 ± 0.08 MPa·m$^{0.5}$ due to small-sized pores inside the micro-pillars. Nonetheless, the fracture toughness values for all specimens measured via Vickers indentation-based testing were lower than the micro-pillar splitting test, owing to the fact that the influence of residual porosity cannot be neglected if larger volume of the material is tested. Lastly, the total conductivity of the specimen cold sintered at 150 °C was close to that of the conventionally sintered specimen at the service temperature of ceramic membranes.

In conclusion, we have demonstrated that carrying out cold sintering of Zr-rich BZCY compositions before the thermal treatment at a higher temperature is an effective synthesis route to achieve superior mechanical properties as compared to traditional high-temperature sintering. Cold sintering of BZCY ceramics offers unique microstructures, but since the research to establish the relationship between the microstructure and mechanical properties is scarce, further exploration in this direction is essential to enhance the mechanical response of the membrane materials under the operating environment. Nevertheless, our research focused on the mechanical properties of the membranes on the micro-scale; however, macro mechanical performance of the size-scaled-up specimens, as well as mechanical behavior at elevated temperatures, is also crucial to assess the material's functionality in real-life working conditions.

CRediT authorship contribution statement

Syed Ali Afzal: Writing – original draft, Investigation, Formal analysis, Data curation. **Moritz Kindelmann:** Writing – review & editing, Methodology, Data curation. **Jürgen Peter Gross:** Writing – review & editing, Resources, Data curation. **Jürgen Malzbender:** Writing – review & editing, Supervision. **Ruth Schwaiger:** Writing – review & editing, Project administration. **Olivier Guillon:** Writing – review & editing, Project administration. **Martin Bram:** Writing – review & editing, Supervision, Conceptualization.

Declaration of competing interest

The authors declare that they have no known competing financial interests or personal relationships that could have appeared to influence the work reported in this paper.

Acknowledgements

Thanks to Dr. Doris Sebold and Dr. Egbert Wessel for the SEM and EDS measurements. Thanks to Dr. Yoo-Jung Sohn for the Rietveld analysis. Special thanks to Mr. Ralf Steinert and Mr. Rakesh Kudupudi for their help during the preparation of specimens. Thanks to German Academic Exchange Service (DAAD) for the financial support (Research Grant ID: 57645448). Lastly, M. Kindelmann is acknowledging funding from the German Science Foundation (DFG) through the grants MA 1280/69-1 and KI 2997/1-1.

Appendix A. Supplementary data

Supplementary data to this article can be found online at https://doi.org/10.1016/j.matdes.2025.114857.

Data availability

Data will be made available on request.

References

[1] C. Duan, et al., Readily processed protonic ceramic fuel cells with high performance at low temperatures, Science 349 (6254) (2015) 1321–1326.
[2] H. Ding, et al., Self-sustainable protonic ceramic electrochemical cells using a triple conducting electrode for hydrogen and power production, Nat. Commun. 11 (1) (2020) 1907, https://doi.org/10.1038/s41467-020-15677-z.
[3] S. Choi, T.C. Davenport, S.M. Haile, Protonic ceramic electrochemical cells for hydrogen production and electricity generation: exceptional reversibility, stability, and demonstrated faradaic efficiency, Energ. Environ. Sci. 12 (1) (2019) 206–215.
[4] C. Duan, et al., Highly durable, coking and sulfur tolerant, fuel-flexible protonic ceramic fuel cells, Nature 557 (7704) (2018) 217–222, https://doi.org/10.1038/s41586-018-0082-6.
[5] S.P.S. Shaikh, A. Muchtar, M.R. Somalu, A review on the selection of anode materials for solid-oxide fuel cells, Renew. Sustain. Energy Rev. 51 (2015) 1–8, https://doi.org/10.1016/j.rser.2015.05.069.
[6] Ali, S.M., et al., Ce0. 80Sm0. 10Ba0. 05Er0. 05O2-δ multi-doped ceria electrolyte for intermediate temperature solid oxide fuel cells. Ceramics International, 2017. 43(1): p. 1265-1271.
[7] Y. Yoo, N. Lim, Performance and stability of proton conducting solid oxide fuel cells based on yttrium-doped barium cerate-zirconate thin-film electrolyte, J. Power Sources 229 (2013) 48–57, https://doi.org/10.1016/j.jpowsour.2012.11.094.
[8] E.M. Sabolsky, et al., SOFC cells and stacks for complex fuels, ECS Trans. 7 (1) (2007) 503.
[9] K. Katahira, et al., Protonic conduction in Zr-substituted BaCeO3, Solid State Ion. 138 (1–2) (2000) 91–98, https://doi.org/10.1016/s0167-2738(00)00777-3.
[10] P. Babilo, T. Uda, S.M. Haile, Processing of yttrium-doped barium zirconate for high proton conductivity, J. Mater. Res. 22 (5) (2007) 1322–1330.
[11] C. Jin, et al., Effect of Ba nonstoichiometry on the phase composition, microstructure, chemical stability and electrical conductivity of BaxCe0.7Zr0.1Y0.1Yb0.1O3−δ (0.9≤x≤1.1) proton conductors, Ceram. Int. 41 (6) (2015) 7796–7802, https://doi.org/10.1016/j.ceramint.2015.02.113.
[12] Z. Liu, et al., Enhancing sinterability and electrochemical properties of Ba (Zr0.1Ce0.7Y0.2)O3-δ proton conducting electrolyte for solid oxide fuel cells by addition of NiO, Int. J. Hydrogen Energy 43 (29) (2018) 13501–13511, https://doi.org/10.1016/j.ijhydene.2018.05.089.
[13] J. Bu, P.G. Jönsson, Z. Zhao, The effect of NiO on the conductivity of BaZr 0.5 Ce 0.3 Y 0.2 O 3− δ based electrolytes, RSC Adv. 6 (67) (2016) 62368–62377.
[14] J. Tong, et al., Cost-effective solid-state reactive sintering method for high conductivity proton conducting yttrium-doped barium zirconium ceramics, Solid State Ion. 181 (11–12) (2010) 496–503.
[15] W. Zhou, et al., Promoting densification and grain growth of BaCe0.65Zr0.2Y0.15O3, J. Mater. Res. Technol. 27 (2023) 3531–3538, https://doi.org/10.1016/j.jmrt.2023.10.180.
[16] Y. Huang, R. Merkle, J. Maier, Effects of NiO addition on sintering and proton uptake of Ba (Zr, Ce, Y) O 3− δ, J. Mater. Chem. A 9 (26) (2021) 14775–14785.
[17] Ashby, M. and K. Johnson, Materials: The Stuff That Surrounds Us, in Materials and Design. 2014. pp. 62–98.
[18] A.J. Nath, R. Lal, A.K. Das, Fired Bricks: CO(2) Emission and Food Insecurity, Glob Chall 2 (4) (2018) 1700115, https://doi.org/10.1002/gch2.201700115.
[19] Randall, C.A., et al., Cold sintering ceramics and composites. 2017, Google Patents.
[20] A. Ndayishimiye, et al., Reassessing cold sintering in the framework of pressure solution theory, J. Eur. Ceram. Soc. 43 (1) (2023) 1–13.
[21] J. Guo, et al., Cold sintering: progress, challenges, and future opportunities, Annu. Rev. Mat. Res. 49 (2019) 275–295.
[22] J.-P. Maria, et al., Cold sintering: current status and prospects, J. Mater. Res. 32 (17) (2017) 3205–3218.
[23] M. Kindelmann, et al., Highly conductive grain boundaries in cold-sintered barium zirconate-based proton conductors, J. Mater. Chem. A 12 (7) (2024) 3977–3988.
[24] J. Gonzalez-Julian, et al., Unveiling the mechanisms of cold sintering of ZnO at 250 C by varying applied stress and characterizing grain boundaries by Kelvin Probe Force Microscopy, Acta Mater. 144 (2018) 116–128.
[25] K. Thabet, et al., High performance dense proton ceramic electrolyte material obtained by cold sintering process, ECS Trans. 91 (1) (2019) 983.
[26] Thabet, K., et al., Application of the cold sintering process to the electrolyte material BaCe0. 8Zr0. 1Y0. 1O3-δ. Journal of the European Ceramic Society, 2020. 40(9): p. 3445-3452.
[27] M. Kindelmann, et al., Cold sintering of BaZr0.7Ce0.2Y0.1O3-δ ceramics by controlling the phase composition of the starting powders, Scr. Mater. 224 (2023) 115147, https://doi.org/10.1016/j.scriptamat.2022.115147.
[28] K. Nur, et al., Mechanical properties of cold sintered ZnO investigated by nanoindentation and micro-pillar testing, J. Eur. Ceram. Soc. 42 (2) (2022) 512–524, https://doi.org/10.1016/j.jeurceramsoc.2021.10.011.
[29] S. Lowum, et al., Mechanical strength of cold-sintered zinc oxide under biaxial bending, J. Mater. Sci. 54 (6) (2019) 4518–4522.
[30] A. Jabr, et al., The effect of liquid phase chemistry on the densification and strength of cold sintered ZnO, J. Eur. Ceram. Soc. 43 (4) (2023) 1531–1541, https://doi.org/10.1016/j.jeurceramsoc.2022.11.071.
[31] S.H. Bang, et al., Toward a size scale-up cold sintering process at reduced uniaxial pressure, J. Am. Ceram. Soc. 103 (4) (2020) 2322–2327.
[32] W. Deibert, et al., Fabrication of multi-layered structures for proton conducting ceramic cells, J. Mater. Chem. A 10 (5) (2022) 2362–2373.
[33] C.A. Schneider, W.S. Rasband, K.W. Eliceiri, NIH image to ImageJ: 25 years of image analysis, Nat. Methods 9 (7) (2012) 671–675, https://doi.org/10.1038/nmeth.2089.
[34] Z. Deng, et al., Elastic properties of alkali superionic conductor electrolytes from first principles calculations, J. Electrochem. Soc. 163 (2) (2015) A67.
[35] K. Niihara, A fracture mechanics analysis of indentation-induced Palmqvist crack in ceramics, J. Mater. Sci. Lett. 2 (5) (1983) 221–223.
[36] P. Chantikul, et al., A critical evaluation of indentation techniques for measuring fracture toughness: II, strength method, J. Am. Ceram. Soc. 64 (9) (1981) 539–543.
[37] J. Tong, et al., Solid-state reactive sintering mechanism for large-grained yttrium-doped barium zirconate proton conducting ceramics, J. Mater. Chem. 20 (30) (2010) 6333–6341.
[38] Z. Shakel, et al., Tailoring the properties of dense yttrium-doped barium zirconate ceramics with nickel oxide additives by manipulation of the sintering profile, Int. J. Energy Res. 46 (15) (2022) 21989–22000.
[39] D. Han, et al., Strategy to improve phase compatibility between proton conductive BaZr 0.8 Y 0.2 O 3− δ and nickel oxide, RSC Adv. 6 (23) (2016) 19288–19297.
[40] P. Castellani, et al., Synthesis of yttrium doped barium zirconate/cerate electrolyte materials and densification using conventional and cold-sintering processes, ECS Trans. 109 (13) (2022) 13.
[41] F. Iguchi, K. Hinata, High-temperature elastic properties of yttrium-doped barium zirconate, Metals 11 (6) (2021) 968, https://doi.org/10.3390/met11060968.
[42] Zeng, Y., et al., Characterization of high Zr/Ce ratio Ba (Zr, Ce, Y) O3-δ proton conductors: investigating the impact of Y on materials properties. Physical Chemistry Chemical Physics, 2024.
[43] J. Bu, P.G. Jönsson, Z. Zhao, Sintering behaviour of the protonic conductors BaZrxCe0.8-xLn0.2O3-δ (x=0.8, 0.5, 0.1; Ln=Y, Sm, Gd, Dy) during the solid-state reactive-sintering process, Ceram. Int. 41 (2) (2015) 2558–2564, https://doi.org/10.1016/j.ceramint.2014.10.177.
[44] D.A. Medvedev, A.A. Murashkina, A.K. Demin, Formation of dense electrolytes based on BaCeO3 and BaZrO3 for application in solid oxide fuel cells: the role of solid-state reactive sintering, Rev. J. Chem. 5 (3) (2015) 193–214, https://doi.org/10.1134/s2079978015030024.
[45] S. Ricote, N. Bonanos, G. Caboche, Water vapour solubility and conductivity study of the proton conductor BaCe(0.9−x)ZrxY0.1O(3−δ), Solid State Ion. 180 (14–16) (2009) 990–997, https://doi.org/10.1016/j.ssi.2009.03.016.
[46] J.-W. Jhuang, et al., Microstructures and electrical properties of zirconium doped barium cerate perovskite proton conductors, Int. J. Hydrogen Energy 44 (38) (2019) 21174–21180.

[47] J. Wallis, et al., The influence of the sintering temperature on BaZr0· 7Ce0· 2Y0· 1O3-δ proton conductors prepared by Spark Plasma Sintering, Ceram. Int. 47 (11) (2021) 15349–15356.
[48] Schaller, R., G. Fantozzi, and G. Gremaud, Mechanical spectroscopy Q [-1] 2001 with applications to materials science. (No Title), 2001.
[49] Pelleg, J., Mechanical properties of ceramics. Vol. 213. 2014: Springer Science & Business.
[50] W. Pabst, E. Gregorová, G. Tichá, Elasticity of porous ceramics—A critical study of modulus–porosity relations, J. Eur. Ceram. Soc. 26 (7) (2006) 1085–1097, https://doi.org/10.1016/j.jeurceramsoc.2005.01.041.
[51] W. Pabst, E. Gregorová, M. Černý, Isothermal and adiabatic Young's moduli of alumina and zirconia ceramics at elevated temperatures, J. Eur. Ceram. Soc. 33 (15–16) (2013) 3085–3093, https://doi.org/10.1016/j.jeurceramsoc.2013.06.012.
[52] J. Malzbender, et al., Measuring mechanical properties of coatings: a methodology applied to nano-particle-filled sol–gel coatings on glass, Mater. Sci. Eng. R: Rep. 36 (2–3) (2002) 47–103.
[53] M. Trunec, Effect of grain size on mechanical properties of 3Y-TZP ceramics, Ceramics-Silikáty 52 (3) (2008) 165–171.
[54] R. Chaim, M. Hefetz, Effect of grain size on elastic modulus and hardness of nanocrystalline ZrO 2-3 wt% Y 2 O 3 ceramic, J. Mater. Sci. 39 (2004) 3057–3061.
[55] R.W. Rice, Grain size and porosity dependence of ceramic fracture energy and toughness at 22 °C, J. Mater. Sci. 31 (8) (1996) 1969–1983, https://doi.org/10.1007/bf00356616.
[56] D.-M. Liu, B.-W. Lin, C.-T. Fu, Porosity dependence of mechanical strength and fracture toughness in SiC-Al2O3-Y2O3 ceramics, J. Ceram. Soc. Jpn. 103 (1201) (1995) 878–881.
[57] A. Moradkhani, et al., Determination of fracture toughness using the area of micro-crack tracks left in brittle materials by Vickers indentation test, J. Adv. Ceram. 2 (2013) 87–102.
[58] T.A. Fabijanić, et al., Vickers indentation fracture toughness of near-nano and nanostructured WC-Co cemented carbides, Metals (2075–4701) 7 (4) (2017).
[59] Q. Liu, A. Roy, V.V. Silberschmidt, Size-dependent crystal plasticity: from micro-pillar compression to bending, Mech. Mater. 100 (2016) 31–40.
[60] C.M. Lauener, et al., Fracture of silicon: influence of rate, positioning accuracy, FIB machining, and elevated temperatures on toughness measured by pillar indentation splitting, Mater. Des. 142 (2018) 340–349.
[61] W. Zhou, et al., Mechanical properties of BaCe0.65Zr0.2Y0.15O3- proton-conducting material determined using different nanoindentation methods, J. Eur. Ceram. Soc. 40 (15) (2020) 5653–5661, https://doi.org/10.1016/j.jeurceramsoc.2020.07.044.
[62] M. Kindelmann, et al., Controlling grain boundary segregation to tune the conductivity of ceramic proton conductors, Adv. Energy Mater. 15 (9) (2025) 2404410.